Final Report

For the Phase I study of

Magnetized Beamed Plasma Propulsion (MagBeam)

Supported by

NASA's Institute for Advanced Concepts

Report Prepared by

R. Winglee and T. Ziemba

Period of Performance

October 1, 2004 to April 30, 2005.

1. Introduction

Electric propulsion has developed rapidly over the last few years. The Deep Space 1 (DS1) spacecraft provided a critical demonstration of the versatility of electric propulsion for space exploration[1]. Launched on Oct. 24, 1998, the spacecraft used a 30-cm ion engine to produce 75 mN of thrust from 2.4 kWe input power. The ion engine uses a cathode/anode system to accelerate electrons to produce ionization of xenon. A negatively biased accelerator grid to accelerate ions to high speeds follows the anode. This system is able to produce a specific impulse (*Isp*) of 3200 s. To avoid the development of a plasma sheath around the spacecraft that would decelerate the ions, a neutralizer outside the engine is used to add electrons so that the ions can escape the spacecraft in charge-neutral plasma. With its high Isp, Deep Space 1's ion engine had efficiencies 10 times that of chemical thrusters. After an acceleration period of 20 months, a ΔV of about 4.5 km/s was obtained for the 1,000-pound spacecraft, using about 80 kg of xenon at $\sim$ 25 sccms and 62% efficiency.

Buoyed by the success of Deep Space 1, there are presently several new NASA initiatives that seek further developments in electric propulsion for spacecraft. NASA Solar System Exploration Roadmap contains several missions requiring large ΔV including the Europa Lander, the Saturn Ring and Titan Observers and the Jupiter Icy Moon Orbiter that require improvements in-space propulsion before their objectives can be met in a cost effective manner. In order to achieve these missions new developments in electric propulsion have to be made. One of the initiatives is NASA's Evolutionary Xenon Thruster (NEXT) [2] under the Next Generation Ion (NGI) initiative for the NASA Code S In-Space Propulsion Program. Another is Project Prometheus, also under the new Code T, which includes the development of nuclear propulsion systems to allow a grand tour of the Galilean moons about Jupiter. A common theme is the need for the propulsion units to provide more total thrust at higher *Isp* (for larger payloads).

In order to achieve higher performance NEXIS will use a 25 kW ion engine similar to DS1 but with the engine size increased to 40 cm diameter. The specific thrust at 35 mN/kW is similar to DS1 but the efficiency is expected to increase from 62% of DS1 to > 68%[2]. However, at 40 cm the system is already becoming relatively massive, and extension to even higher powers becomes problematic due to size and mass restrictions. As more power becomes available for electric propulsion, additional propulsion systems start to have favorable operational characteristics. Hall thrusters uses a radial magnetic field and an induced azimuthal current to produce a $\boldsymbol{J}\times\boldsymbol{B}$ force to accelerate the plasma to high energies. Recent developments in Hall thrusters[3] appear to show marked improvement in efficiencies with 2.3 N attained using 50 kW (specific thrust of 46 mN/kW) at 56% efficiency and a maximum Isp of 2500 s.

An alternative system is the Magnetoplasmadynamic (MPD) thruster. This system has the plasma thrust produced by a radial electric field and an induced azimuthal magnetic field accelerate to produce the accelerated plasma. MPD thrusters[4] have demonstrated high Isp of 2000 for argon and 10000 s for hydrogen. Thrust levels of the order 20 to 100 N using 800 to 4600 kW of power using argon have been reported. Similar thrust levels can be attained for hydrogen but with about twice as much voltage and power being required. These numbers yield a specific thrust of 20-25 mN/kW for argon, which is somewhat less than that for electrostatic ion and Hall thrusters. The efficiencies for argon are low at about 30%, but for hydrogen efficiencies of about 55% are attainable[4]. There is potential that alkali metal and multi-channel cathode MPDs can increase specific thrust levels and efficiencies as well as increase cathode lifetime, which is a significant issue at these power levels.

A different approach that does not use electrodes is the VASIMR[5,6] concept. This concept relies entirely on wave-particle interactions to produce energetic plasma. Breakdown of the plasma is initiated by an RF antenna using 1-3 kW power levels that produces a high intensity whistler wave to produce initial heating of the plasma. Fairly strong magnetic fields of kG to Tesla magnetic fields are used to support the whistler/helicon waves which are driven at 13 MHz. This heating is to be augmented by ion cyclotron heating at megawatt power levels to produce energetic ions, with the conversion of perpendicular ion energy into axial thrust through a magnetic nozzle.

Helicons are important in their own right as high-density plasma sources in a variety of plasma processing applications[6-8]. RF and microwave heating of plasmas has also been proposed as a possible means to increase the efficiency of electric propulsion systems[9-10]. A helicon is also used as the primary plasma source for mini-magnetospheric plasma propulsion (M2P2)[11-12]. More recently, high non-thermal ion flows with energies of the order of 30 eV have be observed in association with helicon plasmas produced in magnetic mirror geometries[13,14]. Results from a high power helicon (HPH) have demonstrated its potential as an electrodeless plasma propulsion system[15,16]. This latter system uses lower frequency (~ 1 MHz) in a few hundred Gauss magnetic field at high densities (of the order of 10^{12} cm^{-3}) so that the energy density of the plasma is comparable to the energy density of the guide magnetic field, i.e. $\beta \sim 1$.

The efficiency of any plasma thruster can potentially be improved by the use of magnetic nozzles. Such magnetic nozzles would use the conservation of the adiabatic invariant to convert thermal energy into directed energy as the plasma moves into decreasing magnetic field. However, an unresolved issue beyond trying to optimized the magnetic nozzle geometry is whether the magnetic field will eventually pull the plasma back along the field lines and into the spacecraft and thereby reduce the efficiency of the system.

If efficient magnetic nozzles can be developed a new application becomes possible, where plasma (and hence power and momentum) can be beamed from one spacecraft to another. The second spacecraft since it does not have to carry the fuel nor the power units can achieve a high ΔV orbits at accelerations 100's of times greater than the ordinary electric propulsion schemes. This beamed-plasma system is hereafter called MagBeam. Because of the high acceleration, new electric propulsion applications become possible including (a) sub-orbital to orbital transfers, (b) low Earth orbit (LEO) to Geosynchronous transfers or escape velocity, and (c) fast planetary missions. Thus, MagBeam offers the potential for greatly enhancing access to space for a broad range of mission scenarios.

The Phase I NIAC research has successfully provided proof-of-concept for MagBeam in terms of (1) computer simulations, (2) initial prototyping laboratory results and (3) trajectory analysis of possible mission scenarios. These results are detailed in the following sections. The computer simulations demonstrate that magnetic nozzles can provide efficient focusing of the plasma but the efficiency is highly dependent on the β of the plasma source and the size of the gradient in the magnetic field. For typical parameters for HPH, excellent focusing is predicted with little return flow into the spacecraft. It is also shown that this same system modifies the pre-existing magnetic field so that there is self-focusing of the plasma beam well beyond the magnetic nozzle. This self-focusing means that long range propagation of the plasma beam can be achieved, which is a primary goal of MagBeam. The physical processes by which self-focusing of the beam can occur are described in Section 2 and the results from comprehensive computer simulations are presented in Section 3.

Section 4 details the laboratory results. These results demonstrate that there is nearly a 50% increase in performance of HPH with the addition of a magnetic nozzle and that the plasma stream is highly focused well down stream from the magnetic nozzle. The laboratory results confirm the self-focusing effects identified in the computer simulations. We demonstrate the usage of the beamed energy to enhance propulsion by using the beamed energy to generate plasma across the change in another magnetic nozzle. Potential missions using MagBeam are described in Section 5 and show that the separation of power/fuel from the payload can produce substantial savings for future space missions. A summary of results is given in Section 6.

2. Self-Focusing Effects in High-β Plasma Streams.

Consider a plasma created near the poles of a dipole-like magnetic configuration as shown in Figure 1a. There are three critical parameters that determine the characteristics of the resultant plasma flow:

(1) the ratio of the bulk speed to the ion thermal speed;

(2) the plasma β which can be broken into two components – β_{Dyn} associated with the dynamic (directed) pressure and β_{Th} due to its thermal pressure;

(3) the ratio of the ion gyroradius relative to the scale length of the magnets.

If the plasma has very low-β (both thermal and dynamic components), the plasma will flow out along the magnetic field lines without making major magnetic field perturbations. The plasma exactly on the pole will be able to escape to infinity but the rest of the plasma will tend to be trapped on close field lines and therefore not contribute to any net thrust on the magnets. As the plasma β is increased a higher fraction of the plasma will escape as it moves into sufficiently weak field that the local β eventually becomes large. The direction of the plasma is highly dependent on the ratio of the ion gyro-radius to the scale length of the magnet. If this ratio is large, the plasma will have random pitch angles as it escapes so that the plasma plume will have a wide opening angle and the directed thrust will not be optimal.

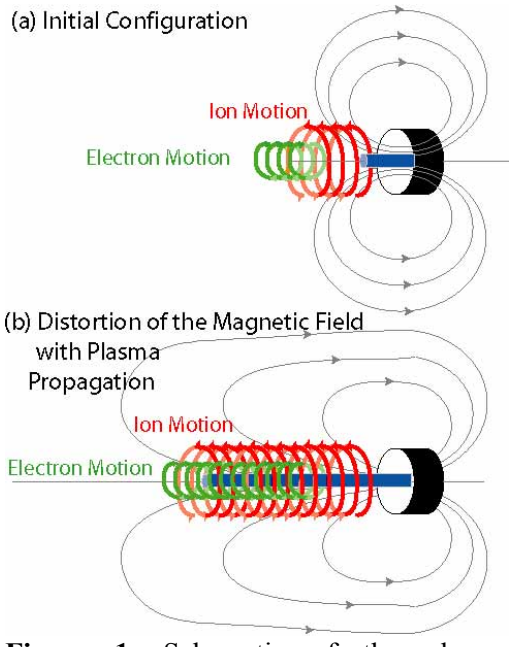

Figure 1. Schematic of the plasma currents and distortion of the magnetic field associated with the beamed plasma.

Instead suppose that at the source $\beta_{Dyn} \sim 1$ and $\beta_{Th} < 1$ and that the ion gyro-radius is smaller than the scale length of the magnets. In this case the plasma has sufficient energy density that it can distort the magnetic field. Through the frozen-in theorem these magnetic field perturbations will lead to the pulling out of the magnetic field as shown in Figure 1b. An equivalent way to think about these magnetic field perturbations is that the electrons rotate in a right hand fashion about the magnetic field, while the ions rotate in the left hand sense. This rotation generates an azimuthal current, particularly in the presence of a beam of finite thickness where edge effects ensure that there is never a full cancellation of the current from adjacent particles as would occur in a homogenous plasma. This azimuthal current leads to the generation of the axial magnetic field that leads to the stretching of the existing magnetic field as shown.

The presence of this axial magnetic field is important since such fields are known to stabilize instabilities that could lead to the disruption of the beam. Since it is the dynamic pressure that is driving the magnetic perturbations and $\beta_{Dyn} > \beta_{Th}$ the thermal energy is insufficient to cause beam expansion and instead is continually converted into the directed energy as the plasma moves into weaker magnetic field.

A critical feature of the system is that with the stretching of the magnetic field, the plasma subsequently injected into the modified field geometry sees a less divergent field. It will therefore experience stronger collimation than earlier injected plasma. This will be true at all times, leading to the self-collimation of the beam (i.e. the collimation from both the magnetic nozzles as well as the induced plasma currents). This effect is demonstrated in the next section through detailed computer simulations.

For the beamed propulsion applications of MagBeam, the presence of an extended magnetic field is a significant advantaged as shown in Figure 2. Suppose that the deflecting system consists of magnet with is dipole axis aligned with the axis of the propulsion system. Magnetic reconnection can occur such that the two magnetic field systems can be tied together which further reinforces the beam confinement. Furthermore, exact aligned of the magnets is not required since reconnection even on the flanks of the deflector will cause the plasma to flow into the poles of the deflecting magnet. Essentially the plasma beam forms a solenoid or magnetic mirror between the two spacecraft. While the magnetic force is attractive, the plasma force dominates and accelerates the spacecraft outward since the β_{Dyn} ($> \beta_{Th}$) > 1.

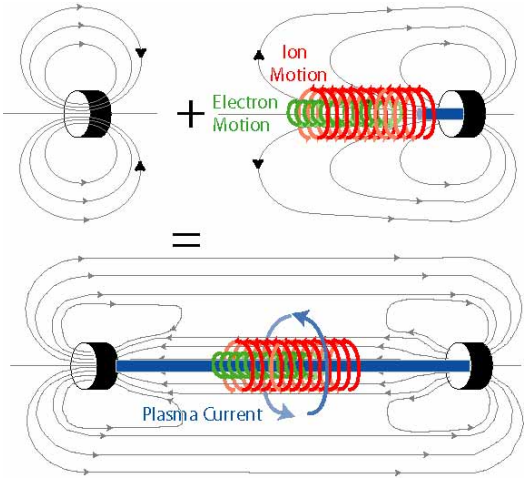

Figure 2. Schematic of the interaction of the beamed plasma with the payload. Due to reconnection the incident plasma will be funneled into the payload and an extended mirror device will be created.

It is the magnetic field embedded within the plasma that makes this system unique from any other beamed particle system because it limits the divergence of the beam, and creates a physical link between the two systems. For an outgoing payload this link will be easy to establish due to the initial close proximity of the two systems. For an incoming payload the angular size at least initially will be small. In order to establish the initial link it may be appropriate to temporarily inflate the magnetic field around the payload spacecraft using M2P2 or plasma magnet technology. When the beamed plasma is funneled into the payload system then the inflation by the payload spacecraft can be switched off so that again there would be only minimal power requirements for the payload during the bulk of the operation of the system.

A schematic of MagBeam is shown in Figure 3. A helicon system is assumed to produce provide the initial plasma. The reason for using a helicon is that it can produce a high density ($> 10^{12}$ cm^{-3}) density that has a highly peaked profile on axis which minimizes losses to the walls in the presence of an axial magnetic field. The magnetic field is produced by the Helmholtz pair around the helicon antenna and is typically 0.2 – 1 kG. To provide collimation of the plasma beam and to ensure escape of the plasma away from the spacecraft a series of additional magnetic nozzle coils are placed in front of the Helmholtz coil. In the schematic two such coils are shown but additional coils could be added in the real application. These coils while larger in

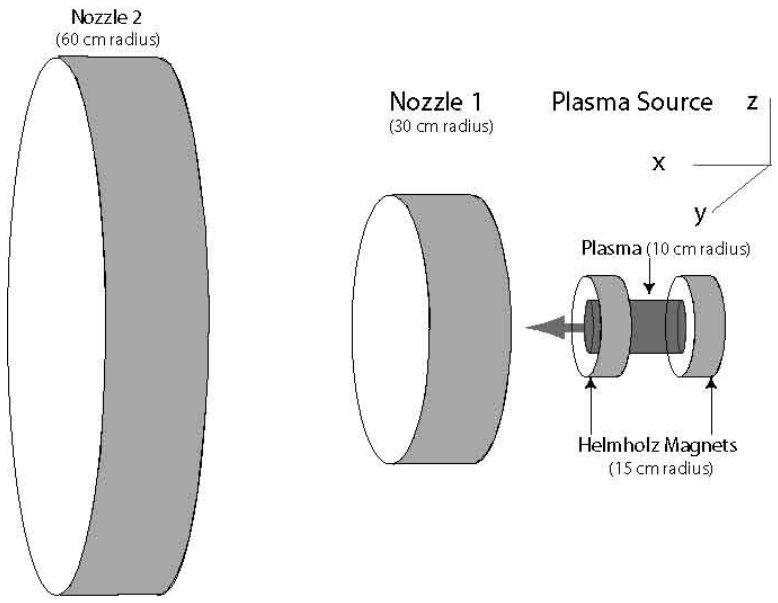

Figure 3. Schematic of the set up of the inner boundary of the simulations system. The source is the same in all the simulations and consists of a pair of Helmholtz coils within which plasma at 2×10^{13} cm^{-3} and $V_b = V_{Th} = 30$ km/s. Various magnetic nozzles are then added to demonstrate change in performance.

area would have weaker magnetic field so that they would not draw substantially more power or require more mass than the Helmholtz coil.

The primary function of the nozzles is provide a magnetic geometry that keeps the plasma as close as possible to the magnetic axis while the plasma moves into weaker magnetic field This ensures the return point of the vacuum magnetic field is at large distances from the spacecraft so that return of plasma is impossible. At the same time the magnet configuration produces a magnetic ramp that causes the bulk of the perpendicular energy of ions and electrons to be converted into parallel energy. This magnetic nozzle increases the efficiency of the thrust generated while minimizing the thermal energy that can lead to beam divergence. In other words the one device simultaneously increases the efficiency of the thrust while at the same time facilitating beaming of plasma energy over large distances. To deflect the beam, the payload spacecraft will have a similar magnet system but it will not need to carry the plasma generation unit nor the required power units.

3. Computer Simulations

3-D multi-fluid simulations are used to quantify the effect of magnetic nozzles near the source and the far field characteristics of the plasma stream. These simulations incorporate ion cyclotron effects in the fluid dynamics and in the induction equation, which are important in examining demagnetization of the ions after exiting the source region. This code is based on extensive modeling of the terrestrial magnetosphere[17-19]. Within the code, the dynamics of each component is given by

$$\frac{\partial \rho_\alpha}{\partial t} + \nabla \cdot (\rho_\alpha \boldsymbol{V}_\alpha) = 0 \tag{1}$$

$$\rho_\alpha \frac{d\boldsymbol{V}_\alpha}{dt} = q_\alpha n_\alpha (\boldsymbol{E}_\alpha + \boldsymbol{V}_\alpha \times \boldsymbol{B}(\boldsymbol{r})) - \nabla P_\alpha \tag{2}$$

$$\frac{\partial P_\alpha}{\partial t} = -\gamma \nabla \cdot (P_\alpha \boldsymbol{V}_\alpha) + (\gamma - 1)\boldsymbol{V}_\alpha \cdot \nabla P_\alpha \tag{3}$$

MHD is based on combining the above equations to give a single-fluid treatment. The multi-fluid treatment is based on the same equations, but the dynamics of the electrons and the different ion species are kept separate. For electrons, it is assumed that they have sufficiently high mobility along the field lines that they are approximately in steady-state drift motion. In

other words, their motion can be described by drift motion (i.e. $d\boldsymbol{V}_{de}/dt = 0$) so that (1) for the electrons reduces to

$$\boldsymbol{E} \quad + \quad \boldsymbol{V}_{de} \times \boldsymbol{B} + \frac{1}{en_e} \nabla P_e = 0 \tag{4}$$

Equation (4) is solved by writing $\boldsymbol{V}_{de}$ in terms of ion velocity and the induced currents assuming quasi-neutrality, i.e.,

$$n_e = \sum_i n_i, \boldsymbol{V}_{de} = \sum_i \frac{n_i}{n_e} \boldsymbol{V}_i - \frac{\boldsymbol{J}}{en_e}, \boldsymbol{J} = \frac{1}{\mu_0} \nabla \times \boldsymbol{B} \tag{5}$$

where the sum of i is over the different ions species that may be present (for example if there is break down of a molecular gas or impurities generated by sputtering). Substitution of (5) into (4) yields the modified Ohm's law of

$$\boldsymbol{E} = -\sum_i \frac{n_i}{n_e} \boldsymbol{V}_i \times \boldsymbol{B} + \boldsymbol{J} \times \boldsymbol{B} + \frac{1}{en_e} \nabla P_e + \eta(x) \boldsymbol{J} \tag{6}$$

The first term in (6) is the ideal Ohm's law, while the second and third terms given the Hall and ∇P corrections (both of which are of order of the ion skin depth relative to the scale length of the system) and the last term $\eta(\boldsymbol{x})\boldsymbol{J}$ is added to allow for finite conductivity regions within the magnet and associated neutral plume near the injection region. Collisions beyond this region are assumed to be negligible.

The description of the electron dynamics is completed by the pressure equation

$$\frac{\partial P_e}{\partial t} = -\gamma \nabla \cdot (P_e \boldsymbol{V}_{de}) + (\gamma - 1) \boldsymbol{V}_{de} \cdot \nabla P_e \tag{7}$$

and the evolution of the magnetic field by the induction equation

$$\frac{\partial \boldsymbol{B}}{\partial t} + \nabla \times \boldsymbol{E} = 0 \tag{8}$$

The plasma electrodynamics is then determined by time stepping (1)-(8) using a second order Runge-Kutta method with flux correction smoothing. The actual configuration of the plasma source and magnetic nozzles is shown in Figure 3. The parameters are chosen to closely resemble those of the laboratory prototype described in the next section. The main different is that the simulations allow much longer scale sizes to be examined than can be considered in the laboratory. The Helmholtz coils for the plasma source are assumed to be 15 cm in radius, and field strength of 200 G. The plasma itself is injected within the magnets with a radius of 10 cm at a density of 2×10^{13} cm^{-3} and a bulk speed of 30 km/s with the thermal speed equal to the bulk speed. For these plasma conditions, the average β in the source region is about 0.5. The grid resolution in this region is 2.5 cm and increases to 1.6 m at large distance from the source. In the following we demonstrate the differences of the above system when a magnetic nozzle is added that has twice the radius of the Helmholtz coils but half the field strength.

The full system size extends about 100 m from the source region. Performance on larger scale sizes can be obtained by simply scaling the present results. However, a more accurate estimate and efficient system could entail additional nozzles as well as higher density sources that would have larger induced plasma currents that incorporated here. A full parameter study of these effects is beyond the scope of the present work.

Figure 4 shows the evolution of the plasma energy density as it propagates out from the Helmholtz coils in the absence of any magnetic nozzles Only the inner part of the simulation

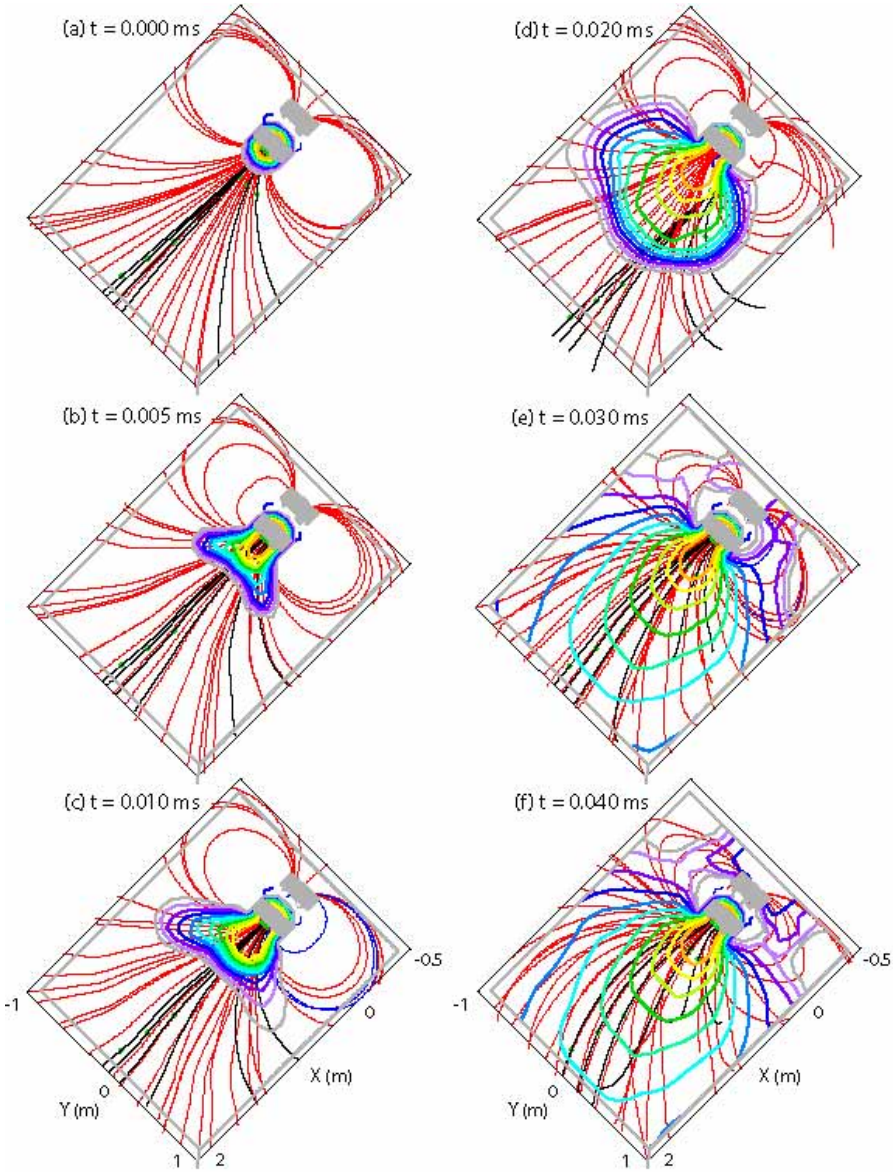

Figure 4. Evolution of the plasma energy density (contour lines of log energy density) and magnetic field (red lines) when only the Helmholtz coil and plasma source is present. Black lines highlight magnetic field lines through fixed points which are shown as green dots. The regions occupied by the Helmholtz coils are shown in grey.

system is shown for clarity. It is seen that there is substantial beam spreading (Figure 4b,c) as the plasma moves out along the magnetic field lines. Some of this plasma is seen to propagate around to the back. However, the bulk of the plasma is able to flow forward, albeit with a very wide opening angle. There is some modification of the magnetic field by plasma induced currents, but the mapping of the magnetic field lines is similar to the vacuum fields.

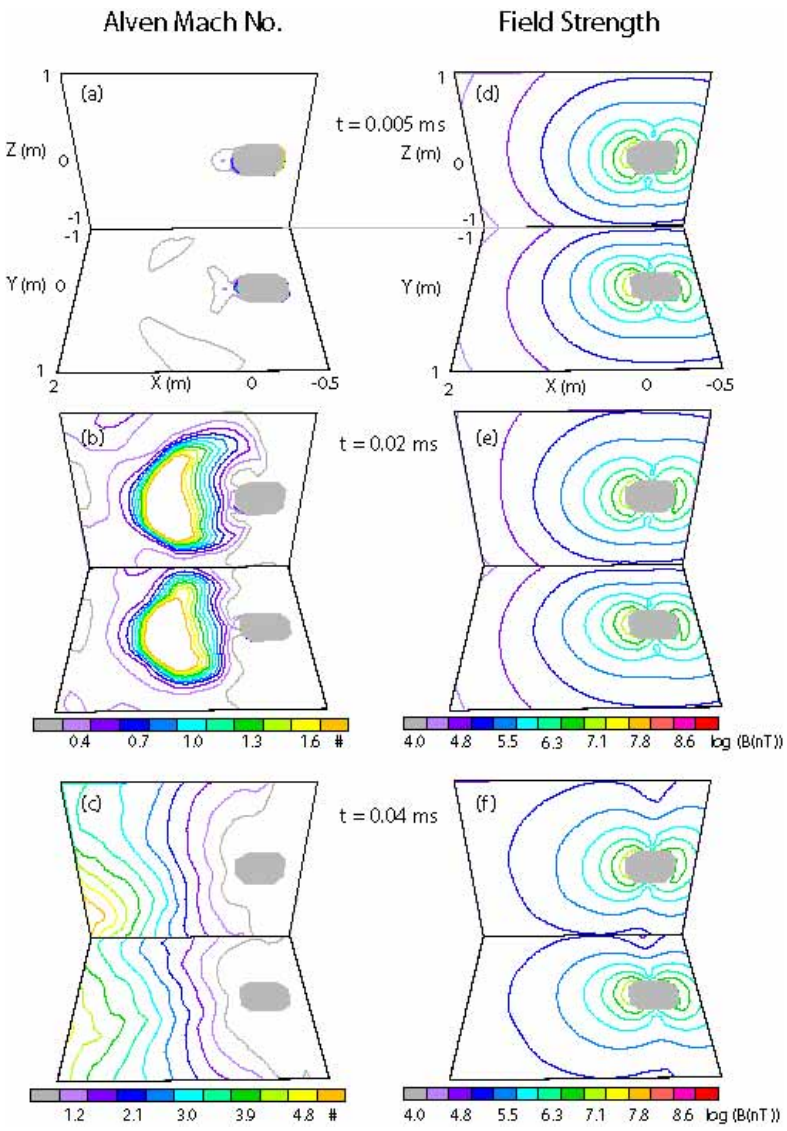

Figure 5. Evolution of the Alfvénic mach number (left hand side) and the magnetic field intensity (right hand side). There is a change in scale on the mach number between panels (b) and (c) to show the differences between the near field (panel b) and the far field (panel c). Contours show slices through a vertical (horizontal) section of the beam on the back (front) sections.

These flow characteristics can be understood by considering the local Alfvén mach number (i.e. the ratio of bulk velocity to the local Alfvén speed) as shown in Figure 5. The number is essentially the square root of β_{Dyn}. At the source the plasma is initially sub-Alfvénic. Since it takes a finite time to fill any flux tube, most of the region away from the source has a very low mach number (Figure 5a) and hence the plasma follows the field lines as noted above. Once the plasma is established on the field lines the mach number rapidly increases above unity due to the very quick falloff in field strength associated with the Helmholtz coil and it is at this stage that the plasma can easily propagate in the forward direction. However, because of the sharp gradients in the magnetic field, the ions are launched at varying angles and this contributes to the wide open angle of the plasma stream. There is some magnetic field variations seen at the latter time (Figures 5c and 5f) but the induced perturbations are only of the order of 10^5 nT (i.e. ~ 1G).

This situation is dramatically changed when a magnetic nozzle is added in front of the plasma source as shown in Figure 6. Similar to Figure 4, there is some initial expansion of the plasma as it leaves the Helmholtz coils (Figure 6b). However, the field from the magnetic nozzle guides the plasma out into the central regions of the magnetic nozzle as seen by the pinching down of the plasma in Figure 6c. As the plasma propagates through the nozzle (Figure 6c) the energy density is very much higher than without the nozzle. There is again some expansion of the beam as it passes beyond the nozzle (Figure 5e) but the bulk of the beam is more strongly collimated over larger scale lengths than in Figure 4. Note that because the beam is still highly focused beyond the nozzle (Figure 5f) there is substantially more bulk velocity in the *x* direction than in the

Helmholtz coil only case in Figure 4. In other words there is a more efficient conversion of plasma energy into directed thrust in the *x*-direction.

An equally important effect of the nozzle is that it concentrates the energy density into the center of the nozzle. At this point the beam radius is only fractionally larger than at the source. However, the magnetic field intensity at the nozzle is less and the gradients in the field slower than at the source region. This means that as the plasma exits the nozzle, it is subject to less divergence that in the Helmholtz only case of Figure 4. This effect is illustrated in Figure 7 where there is a strong beam that develops well beyond the nozzle magnet.

In addition it is seen in Figure 7 that because of the slower falloff in the field, stronger

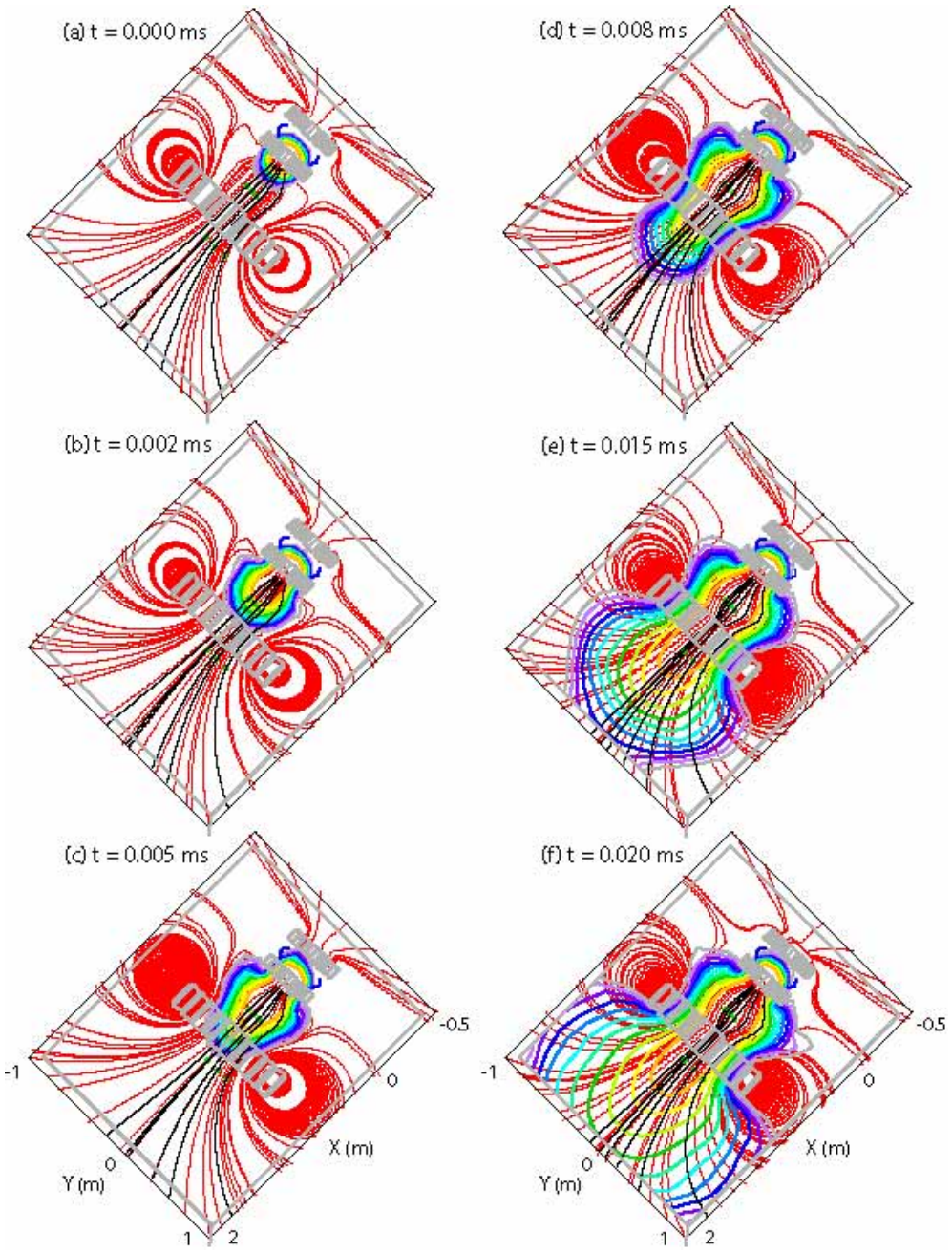

Figure 6. Changes in the beam characteristics when a magnetic nozzle is added to the system.

currents are generated in the plasma. This leads to the pulling in of the flank field lines into the center of the plasma stream (Figures 7b-7d). As a result the subsequent plasma moving out along the field lines sees straighter field lines and are not subject to even less beam divergence (i.e. the plasma is able to produce self-focusing). This self-focusing is seen in Figure 7 for example where the energy density on the flanks of the magnetic nozzle at late times (Figure 7d) is actually less than that in Figure 7b.

Figure 8 shows the asymmetry between the front and back sides of the magnetic nozzle. Due to the funneling effect of the nozzle, the Alfvén mach number is very much larger than unity as the plasma enters the nozzle. This means that the plasma can strongly distort the field lines which is seen as a large increase (10's of G) in the magnetic field intensity beyond the nozzle. This increase is an order of magnitude larger than in Figure 5 despite the fact that the magnetic field intensity is down by a factor of 4 from the source region field strength. It is this change in the field intensity that leads to the pulling in of the magnetic field lines seen in Figure 7.

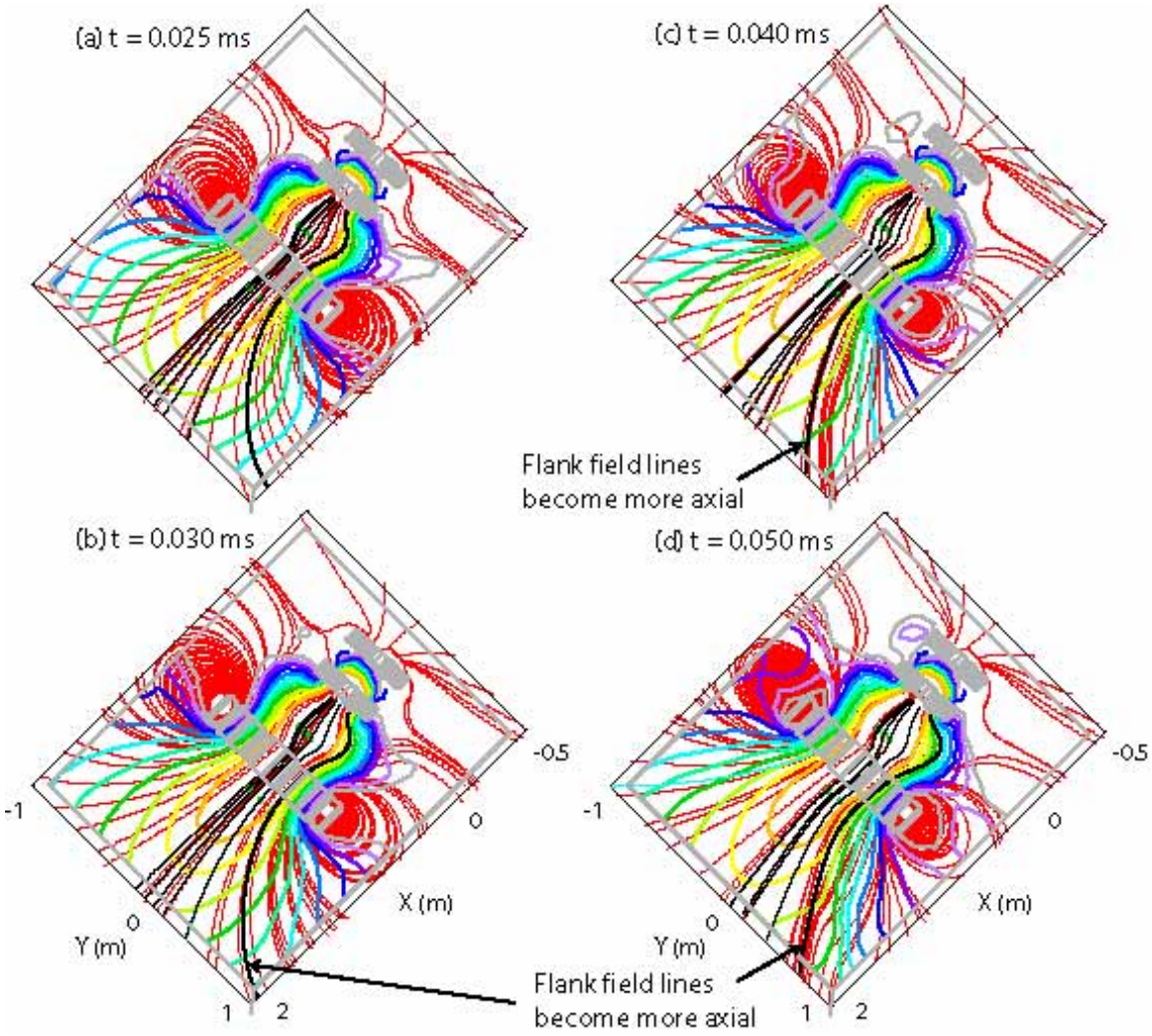

Figure 7. Continuation of Figure 6 showing maintaining of beam integrity and the pulling in of magnetic field lines on the exit side of the magnet nozzle. This change of magnetic topology is due to the induced plasma currents as shown schematically in Figure 2.

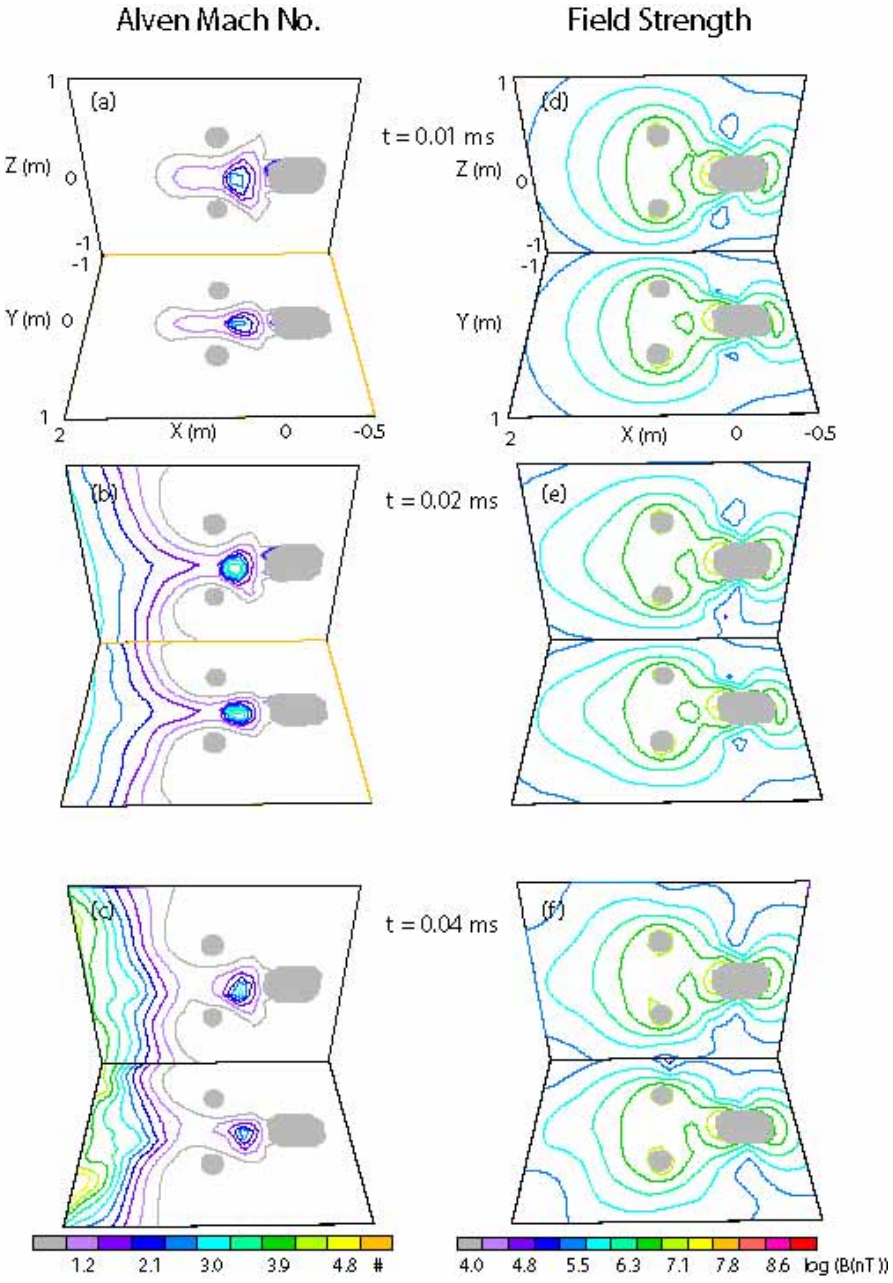

Figure 8. As in Figure 5 except the magnetic nozzle has been added to the system.

When a second magnetic nozzle is added (at twice the distance and radius of nozzle 1 but with 4 times less field intensity) as in Figure 9, the gradient in the magnetic field is reduced even further and this leads to stronger beam convergence through the nozzles. This beam convergence is seen in Figure 9 to be on much larger length scales than the nozzles themselves. This system like the previous system shows some beam divergence as the plasma loads the field lines (Figure 9a and 9b). However, on longer times scales (Figures 9c and 9d) the induced plasma currents are sufficient to fully straighten the magnetic field lines – essentially producing the long solenoid condition of Figures 1 and 2. As these field lines become straight the contours of the beam energy density also straighten, confirming the ability of the plasma to produce its own focusing.

This plasma self-focusing means that the beam propagation over larger distances can be achieved without the typical loss of energy density that typically limits the utilized of other beamed energy configurations (except those using lasers). Furthermore as can be seen in Figure 9 the induced magnetic field is axial which further supports the stability of the plasma beam.

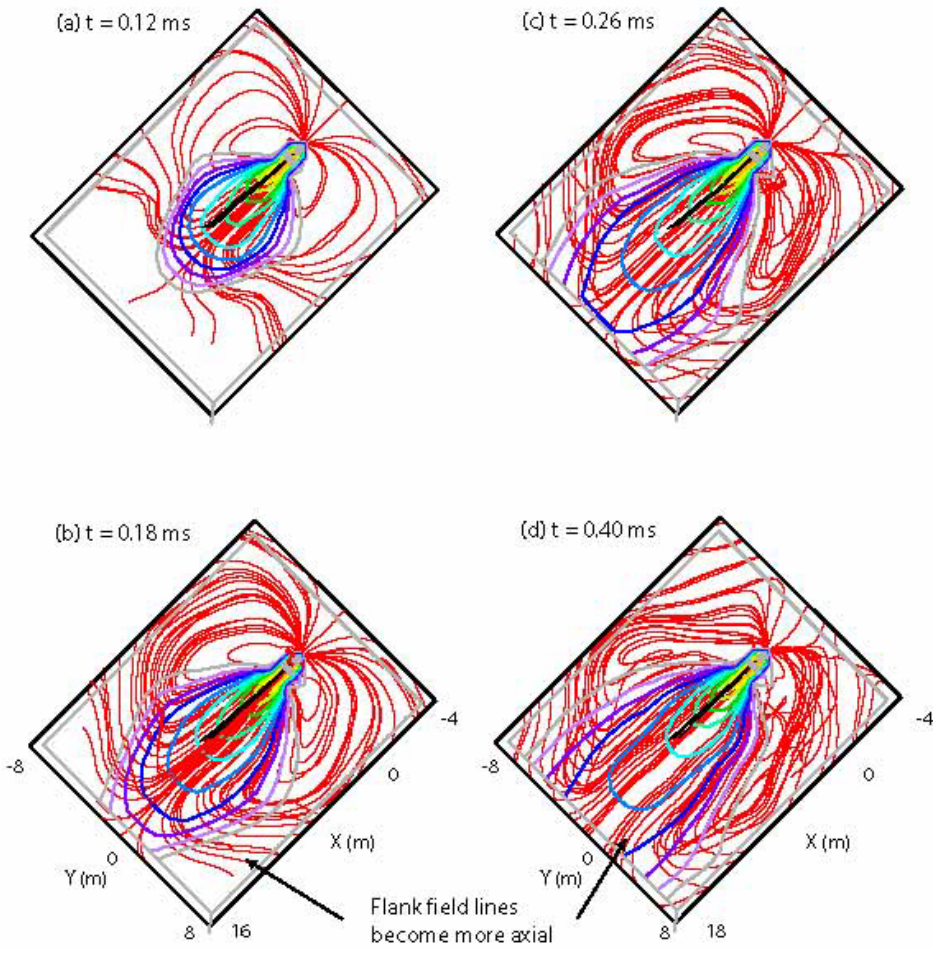

Figure 9. Beam profile and magnetic field profile with the additional of the second magnetic nozzle. Note the scale size is shown is 8 times larger than in the previous Figures.

4. Experimental Validation

Given that the simulations show the potential for self-focusing of the plasma stream, the issue then becomes whether the effect can actually be produced under laboratory conditions. In this section results from the laboratory testing of a prototype are detailed. These results demonstrate that (a) focusing of the plasma stream by magnetic nozzles and (b) self-focusing of the plasma stream once it leaves the magnetic nozzle.

Figure 10. (a) Interior view of the placement of the high power helicon and magnetic nozzles, and (b) exterior view of the experimental setup including the vacuum chamber.

The experimental configuration is shown in Figure 10, and closely resembles the simulation configuration of Figure 3. The system consists of a high power (> 10 kW) helicon (HPH) which is seen at the back of the chamber in Figure 10. HPH uses a Nagoya Type III antenna (7 cm diameter) to create a high intensity rf wave that produces breakdown of the propellant and then heats the electrons to high temperatures (tens of eV). The wave is a non-linear ($\Delta B/B \sim 1$) whistler wave which has its frequency below the electron cyclotron frequency. The electric and magnetic field rotate in the same sense of the electrons in the background field provided by a pair of Helmholtz coils. These coils have an outer diameter of 20 cm, similar to the simulations.

The physical size of HPH antenna is similar to other laboratory helicons, with an outer diameter of 7 cm, and length to 10 cm. It differs in that a solid-state power system enables operation at 300 kHz to 1 MHz at unprecedented powers of 10-100 kW. At these lower frequencies the Helmholtz coils are run at only about 100 G which facilitates a compact design while facilitating limited magnetization of the plasma. At the high input powers, HPH has unique operating characteristics, including higher densities ($> 10^{20}$ m^{-3}), high *Isp's* (2000s for argon, and nearly 4000 s for nitrogen), with high power efficiencies (> 50%) and high neutral gas efficiency (~100%). In all the following data, argon was used as the propellant. The measured plasma β_{dyn} is ~3 within 10 cm of the source. Thus, the nozzle field can magnetically guide the plasma, but the field-line tension is insufficient to pull the plasma back onto the spacecraft, as seen in the computer simulations of the previous section.

Beyond HPH there are two magnetic nozzles. Both nozzles have an outer diameter of 30 cm. Nozzle 1 is in a fixed position of 10 cm from the front of HPH. The purpose of this nozzle is to provide focusing of the HPH plasma. With its magnetic field, the average field within HPH is about 200 G. Nozzle 2 is mounted on a track so that its position can be moved down the length of the chamber. It can be used as an additional focusing magnet (if it is placed close to Nozzle 1)

or it can be used as a deflecting magnetic (if placed at maximal distance at 105 cm from HPH). An array of plasma probes enter from the side of the chamber (which is 6ft long with a 5 ft diameter) that enable the plasma flow to be monitored both along the axis of the chamber and across the chamber.

The mid-chamber Langmuir probe was specially constructed as a flat planar probe that was insulated on one side so that plasma from only one direction is measured. This design enables us to investigate the directivity of the plasma. Essentially no plasma was seen when the collecting area was faced away from HPH. In other words the plasma flow from HPH is highly directional, with very little return flow back onto the system. This is consistent with the model predictions for high-β plasma systems. The only time when significant plasma density is seen in this direction is when xenon gas is injected from the other side of the chamber. In the following, the data from this probe is shown only for the configuration when the collecting surface is facing HPH, i.e. intercepting the HPH plasma stream.

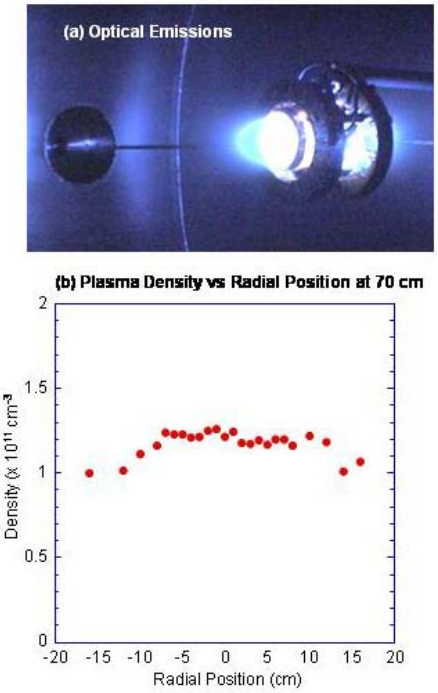

Figure 11. (a) Optical emissions from HPH with no nozzles present and (b) the measured plasma profile at 70 cm downstream from the front of HPH near the end of shot at t = 80 μs.

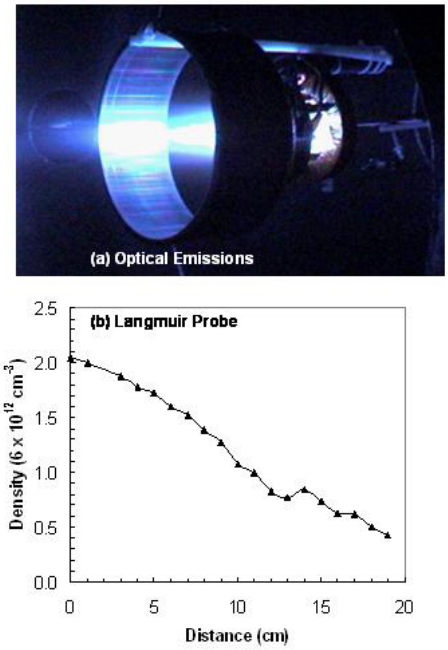

Figure 12. As in Figure 11 but with Nozzle 1 at a mean distance of 10 cm from the front of HPH and with a combined field strength of 210 G. The probe is closer in at 65 cm rather than 70 cm due to the reconfigured system.

Figure 11a shows a close up of HPH operating in the absence of any magnetic nozzles. It is seen that the optical emissions show a peaked profile near the exit of HPH, but within a few cm of the exit the emissions are diffuse with no well defined central plume. These characteristics are verified by Langmuir probe measurements in Figure 11b which shows a radial cut at an axial position of 70 cm from HPH. A very broad profile is seen with a plateau extending ±10 cm and only a relatively small decline in density out to ±20 cm. At this distance the plasma is not tied to the Helmholtz coils but it is also not well collimated.

The change in the operational characteristics with the addition of Nozzle 1 is shown in Figure 12. The optical plume is seen to be substantially elongated and more highly focused. Analysis of the power loading on the antenna shows nearly a 50% increase in the loading which suggests additional energy deposition is occurring at least a wavelength beyond the helicon antenna. The radial profile in this case shows a more peaked profile downstream (Figure 12b). The (half) beam width at 65 cm at half height is about 10 cm. Due to the increased power and collimation of the plasma stream, its density downstream is about a factor of 6 higher than without the magnetic nozzle.

The next step was to determine the change in performance with the addition of the second magnetic nozzle. Two positions where analyzed in detail: (1) at 80 cm which is about 15 cm (i.e. a nozzle radius) downstream from the mid-chamber Langmuir probe at 65 cm, and (2) at 105 cm which is at the far side of the chamber and about 30 cm from the rear-chamber Langmuir probe. These two different configurations are shown in Figure 13. Several different field strengths were investigated. Stronger beam confinement is seen as the field strength is increased. The following results are for Nozzle 2 at 300 G, which is about mid-range of the field strengths investigated.

The difference in configurations can be seen in the figure by the proximity of the mid-chamber feed-through which is just to the right of Nozzle 2 in Figure 13a while it is at the

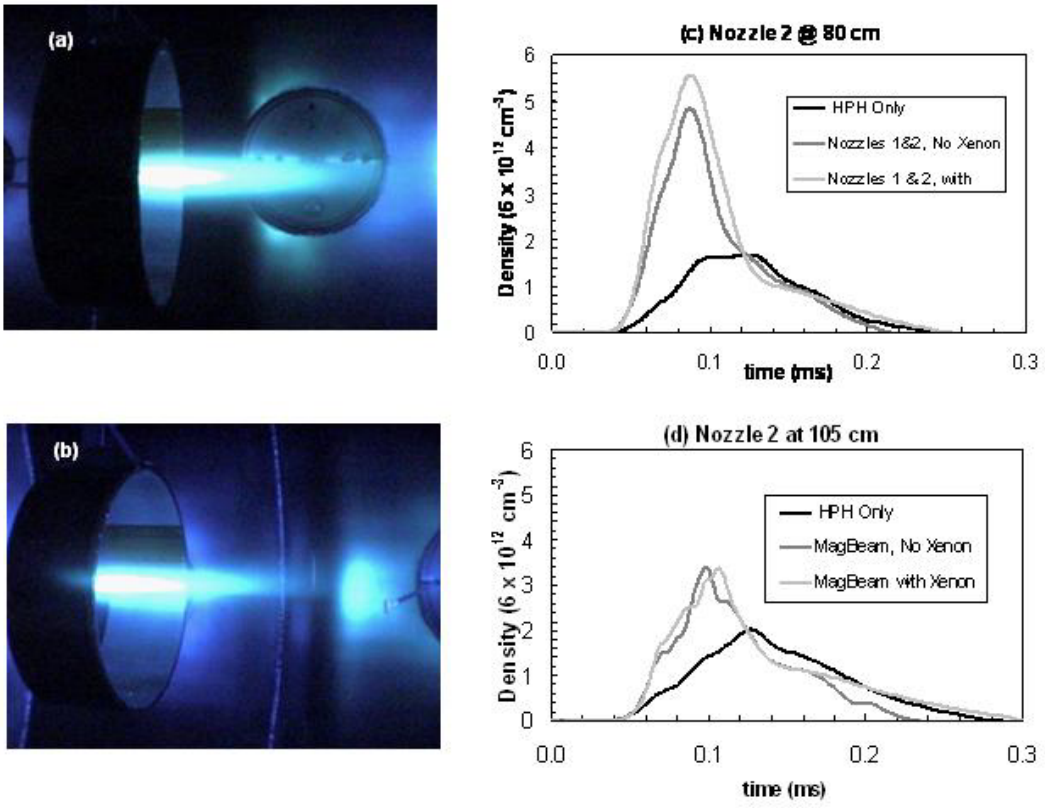

Figure 13. Left hand side shows the optical emissions when xenon is introduced to the middle of the left hand edge of Nozzle 2. Left hand shows the measured plasma densities at the fixed position of 65 m from HPH for the three cases of (a) HPH only (i.e. no nozzle magnets turned on); (b) HPH and Nozzle 1 on, and (c) with everything on with Nozzle 2 at a field strength of 300 G.

extreme right in Figure 1b. The plasma stream at Nozzle 2 is essentially invisible. To aid in the visualization of the plasma stream, xenon gas was puffed into the middle left hand edge on some shots, and it is the optical emissions from these shots that are shown in Figure 13. The use of xenon at Nozzle 2 rather than argon also helps to differentiate the optical emissions from HPH and Nozzle 2 since the xenon gas has a distinctive green component while the argon emissions are essentially blue (particularly for fully ionized systems).

These optical emissions show two important features. First, the electrons from the HPH stream are sufficiently energetic to produce ionization of the xenon gas. This means that we have essentially produced a plasma thruster at Nozzle 2 except that there is no electrical power at Nozzle 2 to create the plasma there. *In other words we have demonstrated that we can indeed separate power from propulsion on a remote system*. Second, in both cases the plasma is highly collimated and in fact the collimation of the xenon stream in Figure 13b appears to be fractionally tighter than in Figure 13a. This means that *we are able to focus essentially all the energy of HPH into Nozzle 2* over extended distances.

The time profiles for the plasma density at the Langmuir probe at 65 cm for the two different configurations are shown in Figures 13c and 13d. As each nozzle is turned on the beam density is seen to increase, consistent with the focusing of the beam as seen in the optical images. Moreover, it is seen that the peak of the emissions is seen to occur earlier, which suggests faster flowing plasma, i.e. there is conversion of bulk thermal energy to directed energy as beam focusing is imposed on the plasma. Measurement of the plasma energy distribution by an electrostatic energy analyzer show increases in speed of about 50% with the addition of Nozzle 1 and another 20% with the addition of Nozzle 2. These changes in bulk speed are consistent with the simulations in the previous section.

The lack of significant changes in the profiles for the system is suggestive that there is some self-focusing of the beam is occurring. A displacement of 25 cm in absolute terms while not large is nearly a full magnet diameter so that if the system were freely expanding significant changes in the plasma density would be expected to be observed and the results do not show such effects. We have used B-dot probes to measure expected plasma-induced magnetic field perturbations predicted by the simulations that would enable self-focusing. The probes have measured perturbations of the order of 10-20 G between the nozzles. The sizes of these perturbations are similar to that seen in the modeling. The problem though is that we do not have the capability of a full 3-D reconstruction of the magnetic field perturbations, and so that these measurements alone cannot be used as definitive evidence for self-focusing.

Evidence for self-focusing comes from the study of the temporal profile of the beam characteristics between the Nozzle 1 and Nozzle 2 (at 65 cm axial distance) versus the downstream characteristics beyond Nozzle 2 (at 130 cm axial distance). As shown in Figure 14, radial cuts at these two fixed axial positions were obtained for two cases: (a) HPH and Nozzle 1 (top panels), and (b) with HPH and Nozzles 1 on and Nozzle 2 located at 80 cm axial distance (bottom panels). Comprehensive profiles for the full duration of the 100 μs shot and into the afterglow out to 200 μs were taken. For the purpose of clarity, only three times slices in the radial profiles at 65 cm are shown while at 130 cm four time slices are shown since there is approximately a 10- 20 μs propagation time from 65-cm probe to the 130-cm probe.

For HPH and Nozzle 1, the radial cross section as already discussed in Figure 12 is well collimated. A beam (half) width at half height at t = 80 μs of about 10 cm is clearly evident at the 65-cm probe. On taking the (half) width at half height at t = 60 μs, a beam width of 7 cm is

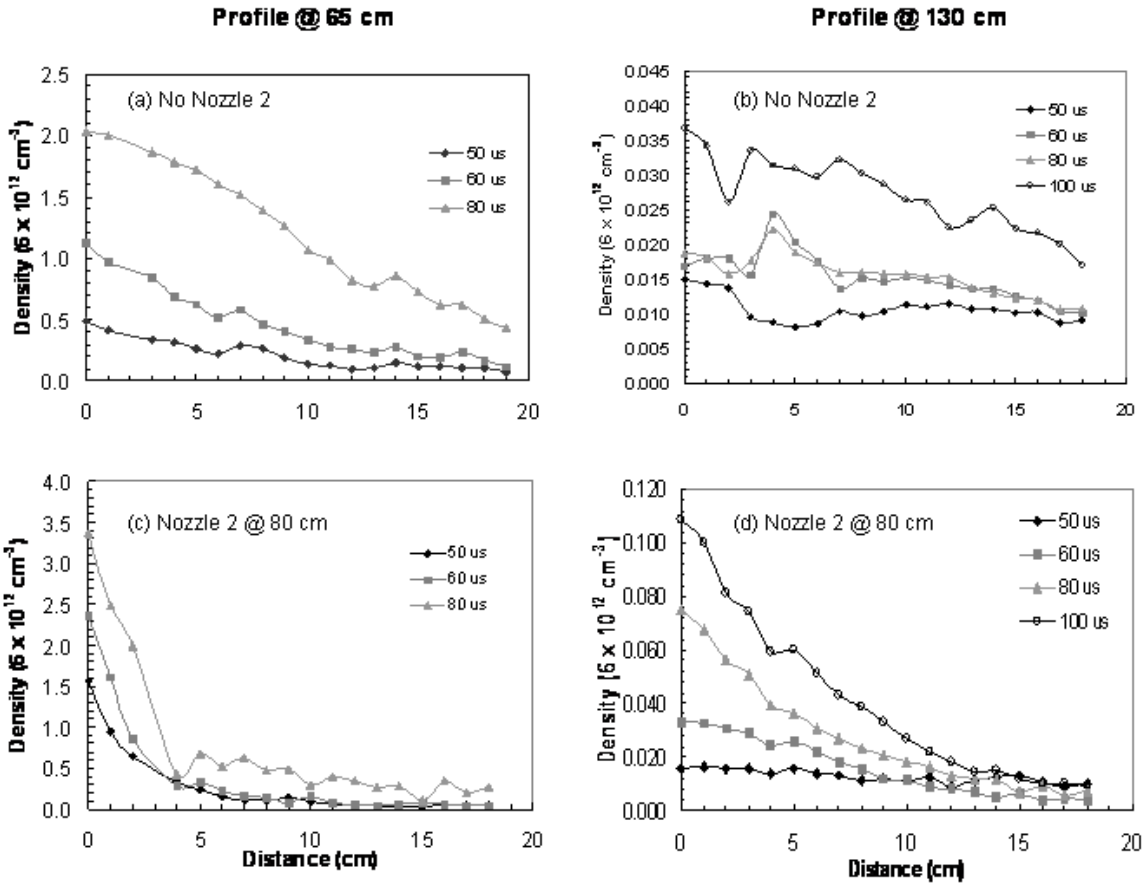

Figure 14. Cross-sections of the beam profile taken at 65 cm (left hand side) and at 130 cm (right hand side) for the HPH and Nozzle 1 (top panels) and with the addition of Nozzle 2 (bottom panels).

obtained. A compilation of the beam widths obtained using this method is shown in Figure 15a, and shows that the beam width at 65 cm probe thickens during the length of the shot. The data at the 130 cm probe shown in Figure 14b shows a much wider profile and much lower plasma density. Because of the lower density there is more shot-to-shot noise but overall the beam width is much wider at about 20 cm. The surprising difference is that the beam thickness at large distances do not track the increasing thickness seen by the probe at 65-cm axial distance. Instead the two thicknesses converge to a single value of 20 cm. If simple beam expansion were occurring then the two profiles should be correlated and convergence to a single beam thickness over large distances should not occur. The fact that beam widths converge shows that plasma effects in addition to the vacuum fields of the magnetic nozzles are influencing the beam expansion.

This effect is even more pronounced when Nozzle 2 is added to the system as shown in the bottom panels of Figure 14. The addition of this nozzle increases the collimation of the beam with a typical half width at half maximum of only a few cm at 65 cm from the source. The actual time evolution of the beam thickness as shown in Figure 15b has an overall profile similar to the no-Nozzle 2 case in Figure 15a but its magnitude is half as small on average. The downstream probe shows an initially very broad profile but this profile actually narrows during the duration

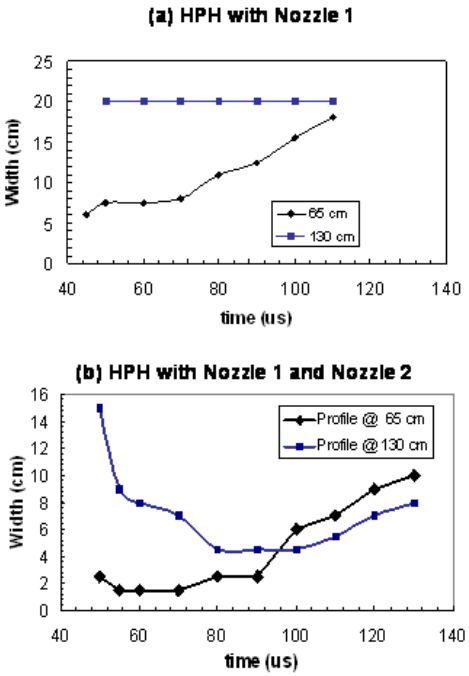

Figure 15. Time evolution of beam profiles for (a) HPH and Nozzle 1 and (b) with the addition of Nozzle 2.

of the shot. Associated with the higher collimation there is an increase in density by a factor of about 3.

As seen in Figure 15b, this additional focusing of the beam actually decreases to a point where it actually appears to have a thinner beam width at 130 cm than at the 65-cm probe. However, if one takes into account the time delay of 10-20 μs between the two probes, the two thicknesses appear to converge to a single value. The key point is that once the plasma discharge is fully developed, *the beam thickness shows no significant divergence with distance down the length of the chamber,* providing strong evidence for self-collimation.

The beam width measured at the 65-cm probe shows thickening of the beam at late times in both cases. This beam thickening eventually shows up at the 130-cm probe at late in the case in Figure 15b. This thickening is probably due to neutral depletion in the source region. At the later times a decrease in plasma density at the source by a factor of about 3-4 is seen near the end of the shot. As a result the plasma density may become sub-Alfvénic at large distances. With such a decrease at the source, the simulations would predict an increase in beam thickness similar to that seen at the later times in Figure 15.

5. Limits on Beam Expansion

With the self-focusing of the plasma beam demonstrated above, long distance propagation of the plasma beam is possible. Naturally occurring beams and even artificial beams[22] in space plasma can propagate hundreds to tens of thousands of km. The main issue that remains is the maximum range possible for MagBeam. We first enumerate these possible limits to the range and then detail possible mission scenarios. These scenarios involve much higher power systems than considered above for very large payloads. It is anticipated that such larger systems would have greater ease in propagating through the local plasma/magnetic fields so that higher power systems are expected to have better propagation characteristics than low power systems.

There are three factors that can control MagBeam's ability to propagate over large distances:

5.1. Plasma Instabilities with the Ambient Plasma. Any beam propagating through a background plasma can be subject to plasma instabilities that can lead to the disruption of the beam. The worse conditions would be when the ambient density is comparable to the beam density. The ionosphere has the highest densities that are likely to be encountered and has a peak density n_{iono} ~ 10^6 cm^{-3} at about 200 km with a maximum ionospheric convection speed V_{conv} ~ 0.5 km/s. Above this altitude the density falls steeply with a scale height of ~ 200 km. Uisng the largest values for the worse case scenario, the number flux entering the beam of length L and radius R is of the order of $n_{iono}\, V_{conv}\, LR$. The number flux from the beam in $n_{beam}\, V_{beam}\, \pi R^2$ where the beam density n_{beam} for the prototype operating 40 kW is of the order of 10^{12}-10^{13} cm^{-3} and a beam speed V_{beam} of 20-50 km/s. Thus the ratio L/R for which the ionospheric density can start to add sufficient density into the beam is of the order of 10^8, so that even a small source has the

capability of propagating a few to several 100's of km. Within magnetosphere the ambient densities is down by 6 orders of magnitude while the convection speed is up 2 orders of magnitude so that tens of thousand km propagation is possible.

5.2. Deflection by the Ambient Magnetic Field. The presence of an ambient magnetic can potentially modify the beam propagation. If the beam propagation is parallel to the beam then the ambient field will actually minimize beam dispersion while if perpendicular it will impede the beam propagation. In the latter case, beam deflection will occur if the beam density becomes low relative to the ambient magnetic field (i.e. low β). As noted above the prototype produces magnetic field perturbations of the order of 20 G downstream from the beam, which is much greater than the terrestrial field at about 0.3-0.4 G at the ionosphere and the 10's nT in the magnetosphere. Thus, the worse conditions are in the ionosphere. If one assumes that self-focusing of the beam occurs at an energy density much higher than the ambient magnetic field energy density then the beam will be able to push the ambient field out of its way once the region is mass loaded by the beam plasma (i.e. when local β becomes greater than unity) so that again long distance propagation is expected.

5.3. Diffusion by anomalous transport. Anomalous transport processes within the beam can also lead to loss of collimation. For the case in point we will assume that the diffusion is Bohm-like, which is the worse case scenario. In laboratory experiments to date[15,16], diffusion rates are a tenth of the Bohm rate so that the following gives a very conservative range. The Bohm diffusion time is given by $T_{Bohm} \sim A/D_{Bohm}$ where $D_{Bohm} = KT_{\perp e}/16\ eB$ is the Bohm diffusion coefficient, $A = \pi R^2$ is the area through which the plasma is diffusing and R and B are the radiii and field strength of the last nozzle magnets. The distance over which the electrons can propagate in this time is

$$L_{Bohm} \sim V_{T_{\|e}} T_{Bohm} = 16\pi R^2 eBV_{T_{\|e}} / KT_{\perp e}. \qquad (9)$$

If one assumes adiabatic invariance then the quantities can be written in terms of their characteristics in the source region, i.e. $\mu = v_\perp^2/B \sim KT_{\perp e}/B$ = constant, and in the source region $KT_{\perp e} \sim KT_{\|e}$. In this limit (9) reduces to $L_{Bohm} \sim 16\pi R^2 / \rho_e$, where ρ_e is the gyroradius of an electron in the source region. For 20 eV plasma, L is of the order of 250 km for R = 10 m and 25000 km for R = 100 m. These distances of a few hundred to a few thousand km for the coherence length are comparable to other processes described above so that Bohm diffusion is not a limiting factor.

6. Orbital and Planetary Transfer Applications.

The above estimates indicate that beam propagation of potentially a few thousand km is possible in the ionosphere and possibly several tens of thousands of km are possible in the magnetosphere. Assuming this type of propagation length, a variety of mission scenarios would be enabled that would provide major cost-savings for NASA. In the following mission scenarios it is assumed that the payload to be moved is 10,000 kg. The MagBeam system is assumed to be on a more massive platform (or space station or for planetary transfer a moon base) since it must carry all the energy and propellant required for orbital transfers. Depending on the application, the high power platform will typically have a mass tens to a hundred times more mass than the payload. As an example of the types of systems available, the International Space Station generates about 100 kW from solar panels. However, these solar panels have a relatively low efficiency of about 6%. Recent developments in triple junction systems have efficiencies of about 30% so that one could reasonably expect this type of system to yield powers of the order of 0.5 MW.

This power level as large as it is is still too small for key applications such as sub-orbital to low Earth orbit (LEO) or a fast geosynchronous (GEO) transfer orbit that minimizes time in the radiation belts for a payload with a mass of the order of 10,000 kg. However, MagBeam does not require the power to be on continuously so that a MW system would in fact be adequate be adequate for MagBeam provided that it was supplemented by a large energy-storage system (either battery or fuel cell for example). Present day batteries have the capacity to store about 400 W hrs/kg (or 1.5 MJ/kg). The theoretical maximum is a factor of 3-4 larger. In the following we will assume only present day storage capacity. Since the power and fuel are no longer carried by the payload, we are no longer subject to the rocket equation, and instead the total power and propellant requirements can be estimated from conservation of momentum arguments:

$$M_{payload}\,\Delta V = 2\,M_{propellant}\,V_{propellant} \tag{10}$$

where the factor of 2 in (12) indicates that the beam is reflected from the payload. More thrust and less power could be achieved if multiple reflections between payload and space station occur. This more efficient configuration is not assumed in the following so we again assume a worse case scenario. The required energy to produce the thrust for this scenario is then given by

$$E_e = 0.5\,M_{propellant}\,V^2_{propellant} = 0.25\,M_{payload}\,\Delta V\,V_{propellant}/\zeta \tag{11}$$

where ζ is the efficiency of converting electrical power into plasma energy. Typical thrusters have efficiencies of the order of 60% as does the HPH system. The power rating for MagBeam is then determined by period in which the payload and space station are in range.

Figure 16a shows the scenario for MagBeam to raise the payload from a sub-orbital to a low Earth orbit (LEO). A relatively high sub-orbital trajectory with an apogee of 300-400 km is required to ensure minimum disruption by the ionosphere while maximizing the interaction time between the payload and the spacestation. The latter is assumed to be in orbit and does an over fly of the suborbital payload. As the two spacecraft approach, MagBeam is assumed to be turned on to give the payload sufficient ΔV of about 3 km/s to put it into LEO. For this low ΔV it is most efficient from an energy stand point to use a relatively low *Isp* propellant of 2000s. For this *Isp* solution of (12) and (13) requires that about 160,000 kg of batteries are required to provide needed energy. Analysis of the orbit trajectories indicates that the interaction time is limited to about 5 min, so that MagBeam must be able to deliver plasma power levels of about 500 MW. There is a back reaction on the orbital characteristics of the spacestation during this period but because the station is very much more massive than the payload, this back reaction is relatively small and can be corrected between payload launches using the MagBeam system as a direct drive system. Alternately a second thruster could be onboard the high power platform to counter MagBeam. However, this would require twice the power and therefore is a more expensive option that just using MagBeam to provide orbit correction at a later time.

In contrast if the same payload were to be launched by a conventional rocket with a propellant speed of 4 km/s then about 20,000 kg of propellant would be required. For these requirements about 10 launches would be required to achieve break even for the cost of the batteries. If one could demonstrate multiple reflections between the plasma source on the spacestation and the payload deflector, then the energy required by the system could be substantially reduced so that breakeven may only require 5 launches.

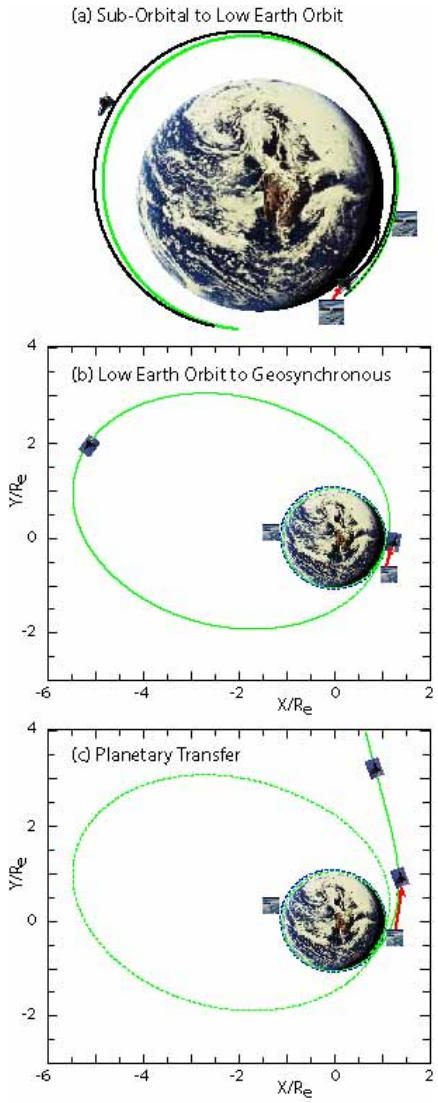

Figure 16. Scenarios for orbital transfers by MagBeam for (a) sub-orbital LEO, (b) LEO to Geosync. transfer, and (c) escape velocity.

The MagBeam system has the additional advantage that it can be used multiple times to continuously raise the orbit of the spacecraft. For example in Figure 16b, at the next rendezvous of the payload and spacestation, MagBeam can be again used to provide an additional 1.5 km/s boost that would move the payload into a geosynchronous transfer orbit. This would be achieved at essentially no cost for MagBeam except for the expenditure of an additional 1000 kg of propellant (less if there are multiple reflections). For chemical rockets, and additional 10,000 kg of propellant would have to be expended for the same orbit. At this point breakeven would require only a few launches.

At the next rendezvous (Figure 16c), another boost of 3 km/s by MagBeam would give the payload escape velocity using the exact same system. At this point a chemical rocket would have required a total 65,000 kg of propellant from the same starting position. As such MagBeam is a very competitive option within 1 or 2 launches to the Moon and beyond. A MagBeam system could also be operated on the surface of the Moon (since there is no atmosphere to affect the propagation of the beam) to provide braking for inbound payloads. This same system could be used in reverse to launch return payloads from the Moon, adding to the total its versatility.

With MagBeam's high acceleration capabilities a fast return mission to Mars is also possible. Such missions though require large ΔV (in excess of 20 km/s from geosynchronous transfer on the outward leg and similar ΔV on the return leg). To meet this ΔV requirement higher energy storage and high speed propellant (*Isp* ~ 4000 s) is required. In addition a long interaction time is required, unless very high accelerations are applied. Assuming the same type of power capabilities as the previous examples, an interaction period of about 4 hrs is required for a few hundred MW plasma system.

This requires that the space station be at a higher orbit. In Figure 17a it is in a high geosynchronous transfer orbit. The height shown is much higher than needed but illustrates the fact that for this large ΔV there is a significant perturbation to the orbit. An equally adequate position for the power system in this case could be a lunar base with the payload receiving the final acceleration as it passes by the Moon or one could have a direct launch from the Moon to Mars. To achieve the necessary ΔV, about 2×10^6 kg of batteries and 7,000 kg of propellant are required.

A similar system is need at Mars to provide breaking. This system would also have to be in high orbit around Mars or on its moon Phobos. Since this system is assumed to be unmanned it

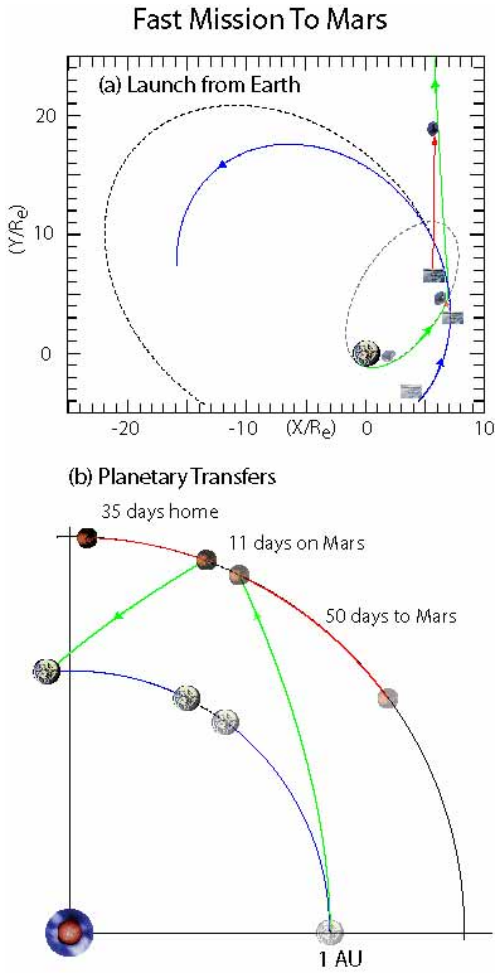

Figure 17. Scenario for fast mission to Mars including (a) Launch from Earth and (b) required planetary alignments.

could be moved to Mars at low speed using its own electric propulsion system along with boosting from the terrestrial system. Return from Mars to Earth would basically use the system in reverse.

For a standard rocket system about 2×10^7 kg of chemical propellant would be required for the outward leg multiplied by the amount of fuel needed to break at Mars. A similar amount would then have to be generated from in-situ resources at Mars for the return leg. The mass of the fuel alone makes this scenario impractical for a chemical rocket system. Thus, MagBeam has the capacity to open up new mission scenarios that are impractical under conventional systems.

The alignment of the planets required for the fast mission is shown in Figure 17b. The Earth is required to be behind Mars, and the high speed of the spacecraft enables it to arrive at Mars before Earth overtakes Mars. If the lag of Earth behind Mars is increased, then longer surface missions are possible. In the example in Figure 17b, a short mission on the surface of 10-11 days is possible. The return mission requires that the spacecraft decrease its orbital velocity around the Sun. For this reason the return leg is shorter than the outward leg since the spacecraft is moving slower. The full duration of the round trip in this scenario is only 96 days.

Finally it should be noted that all the above applications assume a large payload of 10,000 kg. Infrastructure development on Mars or the Moon would be greatly facilitate by the launching of multiple smaller payloads. Such multiple launches would not only enable human exploration of the Moon and Mars but would also enable fast cheap missions to throughout the solar system. For example the higher power required for the fast mission to Mars could equally be used for a fast robotic missions to the outer rim of the solar system (the heliopause) and beyond.

Section 7. Conclusion.

High ΔV orbits that also require high accelerations rates can be achieved by MagBeam by beam the energy from an orbiting infrastructure to the payload. Examples of such missions would include sub-orbital to low Earth orbit (LEO), fast transit through the radiation belts for LEO to geosynchronous orbit or terrestrial escape velocity, and for fast missions to Mars and beyond. The high acceleration is achieved by separating the power and fuel systems from the payload. The high ΔV is obtained through the use of high *Isp* plasma systems. Cost savings come from the fact that plasma systems use substantially less fuel that chemical system, and because the power system is reusable as opposed to needing dedicated power units for each mission. The

magnetic nozzle of the system provides initial focusing of the beam, but unlike charged particle systems, collective plasma processes enable the beam to produce self-focusing and it is this self-focusing that enables long distant propagation of the beam without the usual effects of beam dispersion. In addition, the magnetic field supported by the plasma currents acts to stabilize the plasma beam and further aid its long distance propagation. The ability to produce self-focusing with the MagBeam configuration was demonstrated through both computer simulations and laboratory testing. Further work still needs to be performed to fully elucidate the range of the beam propagation, but at this time all data and estimates suggest that significant distances can be achieved. Demonstration of large distance propagation would confirm the viability of MagBeam and open up major new mission scenario for NASA at greatly reduced cost.

7. References

[1]Polk, J. E., et al., "Validation of the NSTAR ion propulsion system on the Deep Space 1 Mission: Overview and Initial Results," AIAA Paper No. 99-2274, June 1999.

[2]Patterson, M. J., J. E. Foster, T. W. Haag, G. C. Soulas, M. R. Pastel and R. F. Roman, "NEXT: NASA's evolutionary Xenon thruster development status," AIAA Paper No. 2003-4862, July, 2003.

[3]Manzella, D., R. Jankovsky, and R. Hofer, "Laboratory Model 50 kW Hall Thruster," NASA report, 2002.

[4]Choueiri, E. Y., J. K. Ziemer, "Quasisteady magnetoplasmadymanic thruster performance database," *J. Propulsion Power,* **17**, 967, 2001.

[5]Chang-Diaz, F., "Progress on the VASIMR Engine," AIAA paper No. 2003-4997, July, 2003.

[6]Squire, J. P., F. R. Chang-Diaz, T. W. Glovwer, V. T. Jacobson, D. G. Chavers, R. D. Bengtson, E. A. Bering, III, R. W. Boswell, R. H. Goulding and M. Light, 'Progress in experimental research of the VASIMR engine," *Fusion Science and Technology,* **43**, 111, 2003.

[6]D. Miljak and F. Chen, "Density limit in helicon discharges", *Plasma Sources, Sci. and Tech.,* **7,** 537, 1998.

[7]F. Chen, I. Sudit and M. Light, "Downstream physics of the helicon discharge," *Plasma Sources, Sci. and Tech.,* ***5*****,** 173, 1996.

[8]Gilland, J., R. Breun, and N. Hershkowitz, "Neutral pumping in a helicon discharge," *Plasma Sources, Sci. and Tech.,* ***7*****,** 416, 1998.

[9]Patterson, M., M. Domonkos, J. Foster, T. Haag, L. Pinero, G. Soulas, "Ion Propulsion development activities at the NASA Glenn Research Center," AIAA paper No. 2003-4709, July, 2003.

[10]Mori, Y., T. Noutsuka, Y. Takao, H. Nakashima, "ICRF wave propagation and absorption in a microwave discharge ion thruster," *Fusion Science and Technology,* **39**, 195, 2001.

[11]Winglee, R. M., J. Slough, T. Ziemba and A. Goodson, "Mini-magnetospheric plasma propulsion: tapping the energy of the solar wind for spacecraft propulsion," *J. Geophs. Res.,* **105**, 21067, 2000.

[12]Ziemba, T., R. M. Winglee, J. S. Slough, and P. Euripides, "Parameterization of the Laboratory Performance of the Mini-Magnetospheric Plasma Propulsion (M2P2) Prototype," *Proc. of 27th International Electric Propulsion Conference,* **IEPC-01-201**, 2001.

[13]Cohen, S. A., N. S. Siefert, S. Stange, R. F. Boivin, E. E. Scime, and F. M. Levington, "Ion acceleration in plasmas emerging from a helicon-heated magnetic-mirror device," *Physics of Plasmas,* **10**, 2593, 2003.

[14]Conway, G. D., A. J. Perry, and R. W. Boswell, "Evolution of ion and electron energy distributions in pulsed helicon plasma discharges," *Plasma Sources Sci. Tech.,* **7**, 337, 1998.

[15]Ziemba, T., R. Winglee, P. Euripides, L. Giersch, and J. Slough, "Efficient plasma production in low background neutral pressures with the M2P2 prototype," AIAA paper No. 2003-5222, July, 2003.

[16]Ziemba, T., J. Slough, and R. Winglee, "High power helicon propulsion experiments," Space Technology and Applications International Forum-2005, edited by M. S. El_Genk, American Institute of Physics, 2005.

[17]Winglee, R. M., Mapping of ionospheric outflows into the magnetosphere for varying IMF conditions, *J. Atmos., Solar Terrestrial Physics, 62,* 527, 2000.

[18]Winglee, R. M., Circulation of ionospheric and solar wind particle populations during extended southward IMF, *J. Geophys. Res.,108,* 10.1029/2002JA009819, 2003.

[19]Winglee, R. M., Ion cyclotron and heavy ion effects on reconnection in a global magnetosphere, *J. Geophys. Res., 109,* 2004JA010385, 2004.